

Topological nonsymmorphic ribbons out of symmorphic bulk

Augusto L. Araújo,¹ Ernesto O. Wrasse,² Gerson J. Ferreira,¹ and Tome M. Schmidt¹

¹*Instituto de Física, Universidade Federal de Uberlândia, Uberlândia, Minas Gerais 38400-902, Brasil*

²*Universidade Tecnológica Federal do Paraná, Toledo, Paraná 85902-040, Brasil*

(Received 2 December 2015; revised manuscript received 8 March 2016; published 4 April 2016)

States of matter with nontrivial topology have been classified by their bulk symmetry properties. However, by cutting the topological insulator into ribbons, the symmetry of the system is reduced. By constructing effective Hamiltonians containing the proper symmetry of the ribbon, we find that the nature of topological states is dependent on the reduced symmetry of the ribbon and the appropriate boundary conditions. We apply our model to the recently discovered two-dimensional topological crystalline insulators composed by IV-VI monolayers, where we verify that the edge terminations play a major role on the Dirac crossings. Particularly, we find that some bulk cuts lead to nonsymmorphic ribbons, even though the bulk material is symmorphic. The nonsymmorphism yields a new topological protection, where the Dirac cone is preserved for arbitrary ribbon width. The effective Hamiltonians are in good agreement with *ab initio* calculations.

DOI: [10.1103/PhysRevB.93.161101](https://doi.org/10.1103/PhysRevB.93.161101)

I. INTRODUCTION

Topological insulator (TI) materials are characterized by a bulk gap with band inversions and metallic states on the borders. These edge (surface) states are topologically protected by symmetry. A class of TIs protected by time-reversal symmetry has been predicted and realized experimentally [1–5], where a Z_2 topological invariant has been used to characterize them. The crystal lattice symmetry can also lead to topological protection on the topological crystalline insulators (TCIs) [6–13], where the topological nontrivial states are characterized by a crystal symmetry Chern number. Recently, it has been shown that yet a new class of topological nonsymmorphic crystalline insulators [14–20] presenting unique properties with respect to the topological order exists. The overall classification of topological insulators has been discussed based on space group symmetry of the bulk systems [19,21–23]. However, by reducing the symmetry, forming surfaces or edges, a question arises—are the topological protected edge states completely described only by the parent bulk symmetry?

In this Rapid Communication we build effective Hamiltonians using group theory [24–28] for a TCI monolayer and ribbons to investigate the effects of the edge terminations on its topological properties. A PbSe monolayer is chosen as a representative two-dimensional (2D) TCI for our discussion [29–32]. The band structures from the effective Hamiltonians are compared with *ab initio* results obtained from density functional theory (DFT) calculations using the VASP code [33]. We consider five possible crystallographic ribbon cuts, starting from the simpler case A (Fig. 1) building up in complexity towards our main result in ribbon E. We find that the energy dispersion of the topological edge states is strongly dependent on both the reduced symmetry and boundary conditions, resembling graphene's zigzag and armchair edges [34,35]. Interestingly, we show that while our bulk monolayer is a symmorphic lattice, one particular cut leads the nonsymmorphic ribbon E, whose symmetry group is not a subgroup of its bulk counterpart. It is known that nonsymmorphism yields extra degenerescences with respect to its underlying point group [24–28], which in our case results

in an extra protection that preserves the Dirac cone for ribbons of arbitrary width. In addition to the fundamental physics presented here, the nonsymmorphic systems could be potential materials for nanoscale 2D devices, preserving the topological state properties even for nanosized ribbons.

Experimentally, atomic layer growth control of IV-VI materials has been achieved via electrochemical atomic layer epitaxy/deposition [36,37], and PbSe nanorods and nanotubes were recently grown [38]. However, a refined edge control remains as challenging as for any other 2D material. Recently developed chemical bottom-up approaches were successful in graphene [39,40]. Effects of edge saturation and substrates are yet to be experimentally explored. Recently, first-principles calculations showed that the topological properties and the energetic stability of IV-VI monolayers can be manipulated using appropriate substrate [32].

II. MODEL FOR THE INFINITE MONOLAYER

The PbSe monolayer has a square Bravais lattice [Fig. 1(a)] with a space group symmetry D_{4h} . The time-reversal invariant momenta (TRIMs) are Γ , X , Y , and M , as shown in Fig. 1(b). From first principles [29] it is known that the band inversions occur at X and Y , where the symmetry is reduced to the D_{2h} space group. At X , without spin-orbit (SO) couplings the top of the valence band is composed mostly by p_x orbitals of Se, while the bottom of the conduction band is dominated by p_z orbitals of Pb. At Y , all properties are given by a C_4 rotation of X , which allow us to focus our discussion on the X point. To satisfy the Bloch theorem at X the orbitals must be arranged periodically along y and antiperiodically along the x direction, as shown in Fig. 2. To emphasize the Cartesian symmetry of these basis states, we label the kets referring to the axes through which the state is odd. Hence, the states in Figs. 2(a) and 2(b) become $|xz; s\rangle$ and $|x; s\rangle$, respectively. Here $s = \{\uparrow, \downarrow\}$ denotes the spin.

From this set of orbitals, $\{|xz; \uparrow\rangle, |xz; \downarrow\rangle, |x; \uparrow\rangle, |x; \downarrow\rangle\}$, we construct the effective Hamiltonian for the monolayer considering a k -space expansion [34]. Following this ordering, one obtains a matrix representation for the symmetry elements

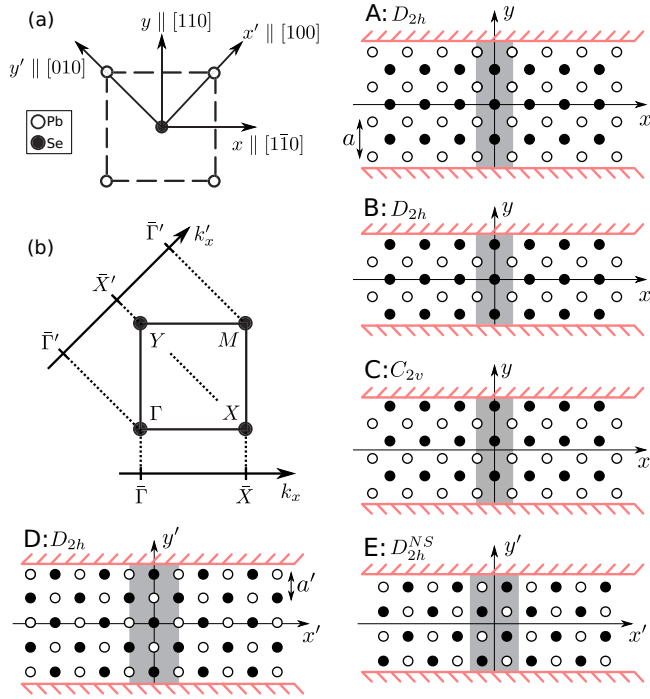


FIG. 1. (a) Unit cell of the PbSe monolayer. (b) The first Brillouin zone (BZ) with the Γ , X , Y , and M TRIMs. Confinement (in red) along y (y') projects the TRIMs onto k_x (k'_x) to form the one-dimensional BZ given by \bar{X} and $\bar{\Gamma}$ (\bar{X}' and $\bar{\Gamma}'$). (A–E) Illustration of the five possible crystallographic terminations of PbSe ribbons. The unit cell of each ribbon is highlighted in gray. The point group symmetries are indicated with usual notation, except for panel E, where “NS” stands for nonsymmorphic. The ribbons considered here have about 45 atoms (~ 10 nm) along y (y').

of the D_{2h} group, plus the time-reversal operator \mathcal{T} [41]. Requiring that the Hamiltonian H_X , for \mathbf{k} around X , commutes with these symmetry elements and \mathcal{T} up to second order in \mathbf{k} , we obtain

$$H_X = \Delta \tau_z + (\alpha_y k_y \sigma_x - \alpha_x k_x \sigma_y) \tau_x + (m_x \tau_z + \delta m_x) k_x^2 + (m_y \tau_z + \delta m_y) k_y^2, \quad (1)$$

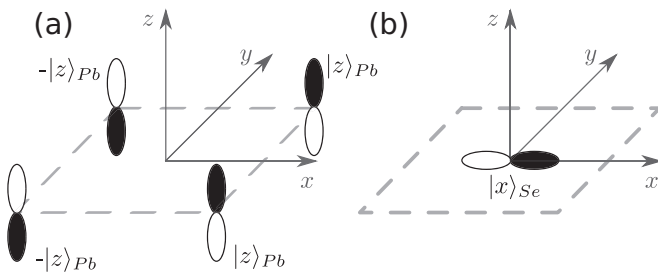


FIG. 2. Representation on the unit cell of the spinless eigenstates of (a) conduction and (b) valence bands at X . The orientation of the p_z orbitals of Pb in (a) are chosen to satisfy the Bloch periodicity at X , and the resulting state $|xz; s\rangle$ is odd along both x and z directions. The state $|x; s\rangle$ in (b) is composed by a single p_x orbital of Se on the unit cell.

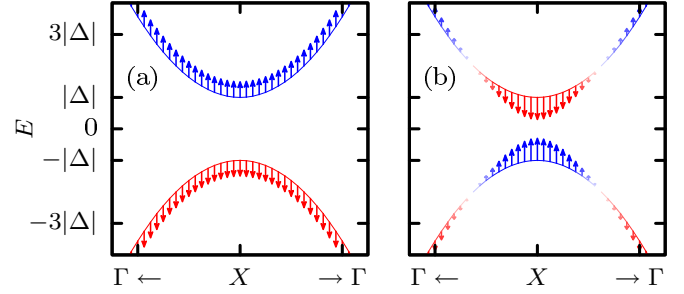


FIG. 3. Band structure of the PbSe monolayer from the effective model for $k_y = 0$ and as a function of k_x . (a) Without SO we consider $\Delta = m_x = 1$, and $\delta m_x = \alpha_x = 0$. (b) With SO the gap changes sign $\Delta = -1$, the masses remain the same, and $\alpha_x = 2$. The colors represent the contributions from the $|x; s\rangle$ (red) and $|xz; s\rangle$ (blue) orbitals in accordance with the *ab initio* data [29]. The arrows represent the spin projection along z .

where the Pauli matrices σ_i (τ_i) act on the spin (orbital) degrees of freedom. From the $k \cdot p$ theory one can associate the α_x and α_y with the k -dependent SO contribution, while the gap Δ has contributions both from the bare lattice potential $V(r)$ and from the k -independent SO term via remote bands. Here Δ plays the role of the Dirac mass and changes sign as a function of the SO intensity. The mass (parabolic) terms $m_{(x,y)}$ are anisotropic, and $\delta m_{(x,y)}$ could break the particle-hole symmetry. This Hamiltonian describes the bulk PbSe monolayer, as we can see in Fig. 3, where the band structure around $k = X$ without ($\Delta = 1$) and with SO couplings ($\Delta = -1$) are in qualitative agreement with *ab initio* data [29].

From the effective bulk Hamiltonian, we can calculate the topological invariants of the system, i.e., the Chern numbers. The bulk monolayer and all possible ribbons share only the identity and mirror \mathcal{M} ($z \rightarrow -z$) symmetry elements. Therefore, all eigenstates belong to one of two classes [11] defined by the eigenvalues $\eta = \pm i$ of the mirror operator, i.e., $\mathcal{M}|\psi_\eta\rangle = \eta|\psi_\eta\rangle$. For each class one defines a Chern number N_η , which allows us to calculate the total Chern number $N_T = N_{+i} + N_{-i}$, and the mirror Chern number $N_{\mathcal{M}} = (N_{+i} - N_{-i})/2$. For $\Delta > 0$ we find all $N_\eta = 0$ and the system is on the trivial regime as expected. For $\Delta < 0$ the states from the occupied bands give $N_{\pm i} = \mp 2$, which yields $N_T = 0$ and $N_{\mathcal{M}} = -2$, thus characterizing the TCI phase [11].

III. TCI RIBBONS

By cutting the monolayer into ribbons, the introduced lateral confinement may break some symmetries of the system, allowing new terms into the effective Hamiltonian. There are two main crystallographic orientations for the ribbons: $x \parallel [1\bar{1}0]$ and $x' \parallel [100]$ directions. The first has three possible edge terminations, illustrated in Fig. 1, panels A, B, and C, while the latter has two more possibilities, shown in Fig. 1, panels D and E. Hereafter we refer to each termination by these capital letters. Next to each panel in Fig. 1 we label the corresponding space group symmetry.

A. Ribbons A, B, AND C

Let us first consider ribbons A, B, and C, which constitute our simplest cases and provide the context to advance to more complex scenarios. First, since ribbons A and B belong to the same D_{2h} space group, they must have the same Hamiltonian $H_A = H_B$. The confinement along y projects Y and Γ into $\bar{\Gamma}$, and M and X into \bar{X} (see Fig. 1). As the bulk gaps at Γ and M are much larger than the gap at X and Y , we can neglect the extra bands coming from these projections. The resulting Brillouin zone of the ribbon is given by the \bar{X} and $\bar{\Gamma}$ TRIMs, whose effective Hamiltonians are obtained replacing $k_y \rightarrow -i\partial/\partial y$ in H_X and $H_Y = C_4 H_X C_4^{-1}$, respectively. Both are in the TCI regime and one can expect topologically protected states at both $\bar{\Gamma}$ and \bar{X} . Second, ribbon C belongs to the C_{2v} space group, which is a subgroup of D_{2h} . However, we find that the extra terms [41] in the Hamiltonian for ribbon C play no significant role in the qualitative analysis of the topological properties discussed here. Hence, its effective Hamiltonian $H_C \approx H_A = H_B$. Ultimately, the distinction between ribbons A, B, and C arises from their different terminations, which enter our effective model via boundary conditions.

To establish the appropriate boundary conditions for the envelope functions for each termination, we extend Brey and Fertig's approach [35] from graphene to our PbSe monolayer ribbon of width $2W$. In ribbon A the edges are composed by Pb atoms, say at $y = \pm W$. If the ribbon was uncut, the next line of atoms on top would be of Se at $y = W + a/2$, where a is the lattice parameter (Fig. 1). Following those, there would be yet a line of Pb atoms at $y = W + a$. However, since those atom lines were cut off to form the ribbon, we set the envelope

function of each sublattice to zero at these positions. A similar definition follows for the bottom edge of ribbon A, and a generalization to ribbons B and C is immediate. Note that the boundary condition for the top edge of ribbon C is equivalent to those of ribbon B, while the bottom of C is equivalent to the boundaries of A.

The resulting band structures of ribbons A, B, and C are shown in the bottom panels of Fig. 4 to be compared with the *ab initio* data on top. We can see some differences between the effective model and the *ab initio* results. First, we observe a band gap at top panels A and B, which is absent from our model (bottom panels). The band gap opening occurs because the ribbon in the DFT calculation is narrow, $2W \approx 10$ nm, and quantum tunnel coupling between topological states from opposite edges takes place. This hybridization gap vanishes asymptotically with the ribbon width. We also observe additional states crossing the Fermi level in the *ab initio* results (upper panels of Fig. 4, panels A–C), due to dangling bonds at the edges.

B. Ribbons D AND E

The other possible terminations occur in ribbons aligned along the (x', y') coordinates, illustrated in Fig. 1, panels D and E, having both Pb and Se atoms at the edges. In these cases we set the envelope functions to zero on the next (absent) line of atoms of both lattices, i.e., at $|y'| = W + a'$, with $a' = a/\sqrt{2}$. Since the boundary conditions for ribbons D and E are the same, their distinction occurs only via the different space groups. Next we show that this translates into distinct XY valley couplings. Interestingly, for ribbon

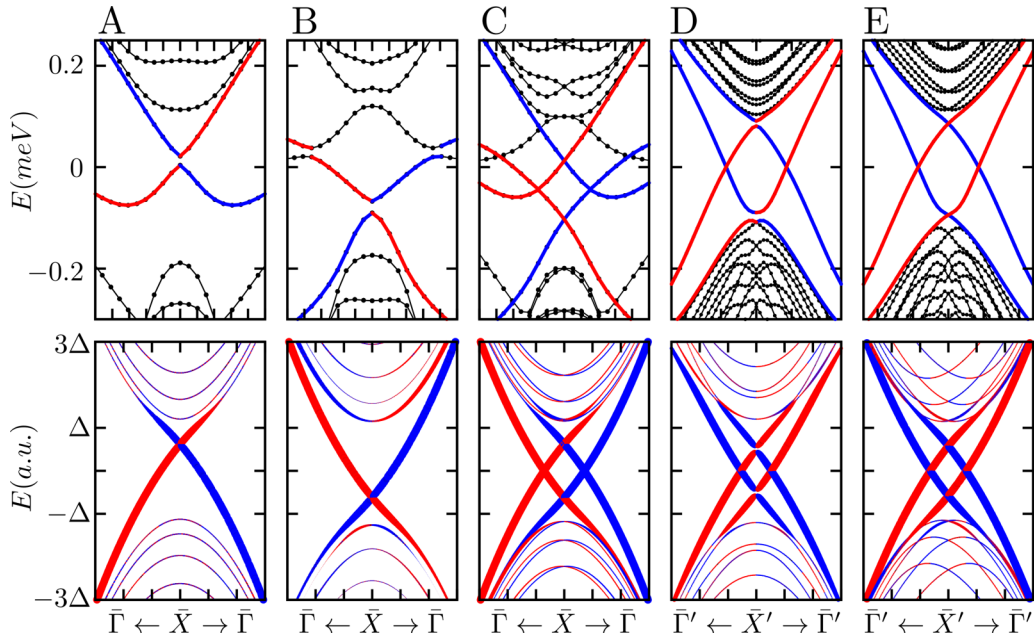


FIG. 4. Comparison of the *ab initio* (top) and effective model (bottom) band structures of PbSe topological insulator ribbons A, B, C, D, and E. The colors represent the spinful mirror parity $+i$ (red) and $-i$ (blue). The thickness of the lines for the effective model represents the localization of the state into an edge. In A, D, and E we show the states and mirror parities projected on the top edge of the ribbons. In B these projections are taken for the bottom edge. In C the upper (lower) Dirac crossing belongs to the top (bottom) edge states. In A, B, D, and E the states shown here are degenerate with ones from the opposite edge, with opposite mirror parity. The *ab initio* data are colored by hand as a guide to the eyes.

E, the nonsymmorphism of the crystal lattice introduces extra topological protections.

Ribbon D belongs to the D_{2h} space group, the same of ribbons A and B. The confinement along y' projects M and Γ into $\bar{\Gamma}$ and both X and Y into \bar{X}' [see Fig. 1(a)]. Therefore one can expect topological states only at \bar{X}' . Since the monolayer bands around Y are simply the ones at X rotated by C_4 , to obtain the effective Hamiltonian around \bar{X}' we have to expand our basis to incorporate the bands coming from Y . Therefore we establish a new matrix representation for the symmetry elements of D_{2h} with a basis set as $\{|xz; \uparrow\rangle, |xz; \downarrow\rangle, |x; \uparrow\rangle, |x; \downarrow\rangle, |yz; \uparrow\rangle, |yz; \downarrow\rangle, |y; \uparrow\rangle, |y; \downarrow\rangle\}$. Following the same procedure discussed previously for H_X , we obtain

$$H_{X'} = \begin{pmatrix} \tilde{H}_X & V_{XY} \\ V_{XY}^\dagger & \tilde{H}_Y \end{pmatrix}, \quad (2)$$

where \tilde{H}_X and \tilde{H}_Y are equivalent to H_X and H_Y rotated towards the \mathbf{r}' coordinates, i.e., $\hat{x} \rightarrow (\hat{x}' - \hat{y}')/\sqrt{2}$, $\hat{y} \rightarrow (\hat{x}' + \hat{y}')/\sqrt{2}$, and equivalent rotations for k_x , k_y , σ_x , and σ_y . The relevant term in the XY valley hybridization V_{XY} for ribbon D is

$$V_{XY} \approx i v_D k_y^2 \tau_z \sigma_z. \quad (3)$$

If V_{XY} were zero, the boundary conditions of ribbon D would give us four degenerate Dirac cones at $E = 0$, leading to eightfold degeneracy (labeled by $\mathcal{M} = \pm i$, X/Y valleys, and top/bottom edges). However, the main contribution to V_{XY} shown in Eq. (3), which is proportional to the mirror symmetry operator $\mathcal{M} = i\tau_z\sigma_z$, couples states from opposite valleys with the same mirror eigenvalue ($\pm i$). This splits the Dirac points into the top and bottom (gapped) cones of Fig. 4, panel D. The hybridization gap opens due to the coupling between top and bottom edge states, which is allowed by Eq. (3), and consistent with the group character tables shown in the Supplemental Material, which guarantees only twofold degeneracy for ribbon D. Other terms of V_{XY} are shown in the Supplemental Material. Their contribution is only quantitative to the fine tuning of the band structure.

Our main result is the unexpected nonsymmorphic space group D_{2h}^{NS} of ribbon E, which yields extra topological protections [19,25]. Here the point group symmetry elements are the same as in D_{2h} , however, some of them must be complemented by a nonprimitive translation $\chi = a'\hat{x}'$ of half a unit cell along x' , i.e., glide planes and screw axis elements [24–28]. To obtain the matrix representation for these symmetry elements we use the same basis set from ribbon D above, but with the coordinates shifted (see Fig. 1). Requiring that the Hamiltonian commutes with these elements and \mathcal{T} , we obtain again $H_{X'}$, but with different XY valley couplings V_{XY} , whose relevant terms for ribbon E are

$$V_{XY} \approx v_E k_y^2 (i\tau_x\sigma_y - \tau_y\sigma_x). \quad (4)$$

Similarly to ribbon D, this XY valley coupling splits the otherwise eightfold degeneracy into the top and bottom Dirac cones of Fig. 4, panel E. Here they remain gapless. Other terms of V_{XY} compatible with the symmetries of ribbon E contribute only with the fine tuning of the band structure. These are shown in the Supplemental Material.

We emphasize that the edge state dispersions for ribbons D and E, shown in Fig. 4, panels D–E, differ only by the hybridization gaps at X , which is the main consequence of the nonsymmorphic lattice of ribbon E. Here, all edge state branches are doubly degenerate with states located at opposite edges having opposite mirror parities. The color code in the figure refers to the states located on the top edge. Therefore, at each crossing around X' there are four states. The agreement between the effective Hamiltonian and the *ab initio* results is patent. In ribbon D the gap between edge branches is a consequence of top/bottom edge hybridization for narrow ribbons. The gap is closed in the nonsymmorphic ribbon E, which is consistent with its double group character table [41]. We have calculated this character table using standard group theory method [25] to find that the double group is composed by two-dimensional irreducible representations (IRREPs), which yields twofold degeneracies. However, while for ribbons A, B, C, and D the time-reversal symmetry does not lead to extra degeneracies, for ribbon E the pair of 2D IRREPs form Kramers partners. This leads to the fourfold degeneracy of the edge states of ribbon E at X' , which *must survive even for narrow ribbons or arbitrary width, despite the overlap between top and bottom edge states*. Usual edge state branches, as in ribbon D, can only close the gap asymptotically for wide ribbons, constituting an accidental degeneracy, which is not protected by symmetry.

IV. FINAL REMARKS AND CONCLUSIONS

The double crossing band structure of ribbon C resembles those of D and E, with closed gaps. However, here edge state branches are nondegenerate. The bottom crossing at X corresponds to a pair of opposite mirror parity states coming from the top edge, which are equivalent to half of the edge states of ribbon B. Similarly the top crossing at X involves states from the bottom edge of ribbon C, which are equivalent to half of the states of ribbon A. Consequently, the crossings of pairs of edge states from opposite sides are already split in energy, thus avoiding a direct hybridization, which keeps the gap closed, in contrast to its counterparts in ribbons A and B.

Interestingly, the gap oscillation with even/odd number of layers recently reported in Ref. [13] originates in the alternation between symmorphic and nonsymmorphic lattices in three dimensions, which can be understood as a 3D counterpart of our results.

In conclusion, we showed that, although the Chern number and topological classification of insulators remain a bulk property, the reduced symmetry of the ribbons and the characteristics of its edge terminations play a fundamental role in the topological state properties. Particularly, we focused on the TCIs given by IV–VI monolayers, whose pair of distinct atoms lead to distinct sublattices, similarly to graphene. While different cuts of the bulk in graphene give us the armchair and zigzag ribbons, here we identify five main types of ribbons due to the more complex structure of the lattice. Interestingly, we find that the extra topological protection introduced by nonsymmorphic symmetry yields protected crossings for ribbons of arbitrary width. This is in contrast with the usual topological protections, where the gaps are only asymptotically closed for large enough samples. The

extra nonsymmorphic protection of the ribbon could not be predicted by the bulk topological classification, since the bulk is symmorphic. This feature may allow topological properties to be explored in nanoscale nonsymmorphic TIs.

ACKNOWLEDGMENTS

The authors acknowledge the financial support from the Brazilian Agencies CNPq, CAPES, and FAPEMIG, and the computational facilities from CENAPAD.

-
- [1] C. L. Kane and E. J. Mele, *Phys. Rev. Lett.* **95**, 146802 (2005).
- [2] B. A. Bernevig, T. L. Hughes, and S.-C. Zhang, *Science* **314**, 1757 (2006).
- [3] M. König, S. Wiedmann, C. Brüne, and A. Roth, *Science* **318**, 766 (2007).
- [4] D. Hsieh, D. Qian, L. Wray, Y. Xia, Y. S. Hor, R. Cava, and M. Z. Hasan, *Nature (London)* **452**, 970 (2008).
- [5] M. Z. Hasan and C. L. Kane, *Rev. Mod. Phys.* **82**, 3045 (2010).
- [6] L. Fu, *Phys. Rev. Lett.* **106**, 106802 (2011).
- [7] T. H. Hsieh, H. Lin, J. Liu, W. Duan, A. Bansil, and L. Fu, *Nat. Commun.* **3**, 982 (2012).
- [8] Y. Tanaka, Z. Ren, T. Sato, K. Nakayama, S. Souma, T. Takahashi, K. Segawa, and Y. Ando, *Nat. Phys.* **8**, 800 (2012).
- [9] P. Dziawa, B. Kowalski, K. Dybko, R. Buczko, A. Szczerbakow, M. Szot, E. Łusakowska, T. Balasubramanian, B. M. Wojek, M. Berntsen, O. Tjernberg, and T. Story, *Nat. Mater.* **11**, 1023 (2012).
- [10] Y. Okada, M. Serbyn, H. Lin, D. Walkup, W. Zhou, C. Dhital, M. Neupane, S. Xu, Y. J. Wang, R. Sankar, F. Chou, A. Bansil, M. Z. Hasan, S. D. Wilson, L. Fu, and V. Madhavan, *Science* **341**, 1496 (2013).
- [11] Y. Ando and L. Fu, *Annu. Rev. Condens. Matter Phys.* **6**, 361 (2015).
- [12] S.-Y. Xu, C. Liu, N. Alidoust, M. Neupane, D. Qian, I. Belopolski, J. Denlinger, Y. Wang, H. Lin, L. Wray *et al.*, *Nat. Commun.* **3**, 1192 (2012).
- [13] H. Ozawa, A. Yamakage, M. Sato, and Y. Tanaka, *Phys. Rev. B* **90**, 045309 (2014).
- [14] S. A. Parameswaran, A. M. Turner, D. P. Arovas, and A. Vishwanath, *Nat. Phys.* **9**, 299 (2013).
- [15] C.-X. Liu, R.-X. Zhang, and B. K. VanLeeuwen, *Phys. Rev. B* **90**, 085304 (2014).
- [16] K. Shiozaki, M. Sato, and K. Gomi, *Phys. Rev. B* **91**, 155120 (2015).
- [17] C. Fang and L. Fu, *Phys. Rev. B* **91**, 161105 (2015).
- [18] D. Varjas, F. de Juan, and Y.-M. Lu, *Phys. Rev. B* **92**, 195116 (2015).
- [19] S. M. Young and C. L. Kane, *Phys. Rev. Lett.* **115**, 126803 (2015).
- [20] Y. Chen, H.-S. Kim, and H.-Y. Kee, [arXiv:1512.08865](https://arxiv.org/abs/1512.08865).
- [21] R.-J. Slager, A. Mesaros, V. Juričić, and J. Zaanen, *Nat. Phys.* **9**, 98 (2013).
- [22] C. Fang, M. J. Gilbert, and B. A. Bernevig, *Phys. Rev. B* **86**, 115112 (2012).
- [23] P. Jadaun, D. Xiao, Q. Niu, and S. K. Banerjee, *Phys. Rev. B* **88**, 085110 (2013).
- [24] L. Voon and M. Willatzen, *The k.p Method: Electronic Properties of Semiconductors* (Springer, Berlin/Heidelberg, 2009).
- [25] M. Dresselhaus, G. Dresselhaus, and A. Jorio, *Group Theory: Application to the Physics of Condensed Matter* (Springer, Berlin/Heidelberg, 2007), SpringerLink: Springer e-Books.
- [26] R. Car, G. Ciucci, and L. Quartapelle, *J. Math. Phys.* **17**, 1051 (1976).
- [27] G. F. Koster, *Space Groups and Their Representations* (Academic Press, New York, 1957).
- [28] K. Watari and A. Fazzio, *Introdução a Teoria de Grupos: Aplicada em Moléculas e Sólidos* (Ed. UFSM, Santa Maria, 1998).
- [29] E. O. Wrasse and T. M. Schmidt, *Nano Lett.* **14**, 5717 (2014).
- [30] J. Liu, X. Qian, and L. Fu, *Nano Lett.* **15**, 2657 (2015).
- [31] C. Niu, P. M. Buhl, G. Bihlmayer, D. Wortmann, S. Blügel, and Y. Mokrousov, *Phys. Rev. B* **91**, 201401 (2015).
- [32] K. Kobayashi, *Surf. Sci.* **639**, 54 (2015).
- [33] G. Kresse and J. Furthmüller, *Phys. Rev. B* **54**, 11169 (1996).
- [34] D. P. DiVincenzo and E. J. Mele, *Phys. Rev. B* **29**, 1685 (1984).
- [35] L. Brey and H. A. Fertig, *Phys. Rev. B* **73**, 235411 (2006).
- [36] R. Vaidyanathan, J. L. Stickney, and U. Happek, *Electrochim. Acta* **49**, 1321 (2004).
- [37] R. Vaidyanathan, S. M. Cox, U. Happek, D. Banga, M. K. Mathe, and J. L. Stickney, *Langmuir* **22**, 10590 (2006).
- [38] H. Li, J. Yang, C. Liang, W. Zhang, and M. Zhou, *Appl. Surf. Sci.* **258**, 8959 (2012).
- [39] A. Narita, X. Feng, and K. Müllen, *Chem. Rec.* **15**, 295 (2015).
- [40] R. M. Jacobberger, B. Kiraly, M. Fortin-Deschenes, P. L. Levesque, K. M. McElhinny, G. J. Brady, R. R. Delgado, S. S. Roy, A. Mannix, M. G. Lagally, P. G. Evans, P. Desjardins, R. Martel, M. C. Hersam, N. P. Guisinger, and M. S. Arnold, *Nat. Commun.* **6**, 8006 (2015).
- [41] See Supplemental Material at <http://link.aps.org/supplemental/10.1103/PhysRevB.93.161101> for the matrix representation of the symmetry elements, and character tables of space groups.